Single-shot transverse coherence in seeded and unseeded free-electron lasers: A comparison

M. Pop,[1,*] E. Allaria,[2] F. Curbis,[1] G. Geloni,[3] M. Manfredda,[2] S. Di Mitri,[2] L. Foglia,[2] D. Garzella,[4] L. Giannessi,[2,5] B. Mahieu,[6] N. Mahne,[7] N. Mirian,[2] G. Penco,[2] G. Perosa,[2,8] P. R. Ribič,[2] A. Simoncig,[2] S. Spampinati,[2] C. Spezzani,[2] M. Trovò,[2] S. Werin,[1] M. Zangrando,[2,7] and G. De Ninno[2,9,†]

[1]*Physics department, Lund University, 22100 Lund, Sweden*
[2]*Elettra-Sincrotrone Trieste, 34149 Basovizza, Trieste, Italy*
[3]*European XFEL, 4 Holzkoppel 4, 22869 Schenefeld, Germany*
[4]*LIDYL, CEA, CNRS, Université Paris-Saclay, CEA Saclay, 91191 Gif-sur-Yvette, France*
[5]*ENEA C.R. Frascati, Via E. Fermi 45, 00044 Frascati (Roma), Italy*
[6]*Laboratoire d'Optique Appliquée, ENSTA ParisTech, CNRS, Ecole Polytechnique, Université Paris-Saclay, 91762 Palaiseau Cedex, France*
[7]*Istituto Officina dei Materiali, Consiglio Nazionale delle Ricerche, Basovizza, Italy*
[8]*University of Trieste, Dipartimento di Fisica, Piazzale Europa 1, 34127 Trieste, Italy*
[9]*Laboratory of Quantum Optics, University of Nova Gorica, 5001 Nova Gorica, Slovenia*

(Received 14 January 2022; accepted 10 March 2022; published 6 April 2022)

The advent of x-ray free-electron lasers (FELs) drastically enhanced the capabilities of several analytical techniques, for which the degree of transverse (spatial) coherence of the source is essential. FELs can be operated in self-amplified spontaneous emission (SASE) or seeded configurations, which rely on a qualitatively different initialization of the amplification process leading to light emission. The degree of transverse coherence of SASE and seeded FELs has been characterized in the past, both experimentally and theoretically. However, a direct experimental comparison between the two regimes in similar operating conditions is missing, as well as an accurate study of the sensitivity of transverse coherence to key working parameters. In this paper, we carry out such a comparison, focusing in particular on the evolution of coherence during the light amplification process.

DOI: 10.1103/PhysRevAccelBeams.25.040701

I. INTRODUCTION

Several analytical techniques, such as coherent diffractive imaging [1], Fourier transform holography [2] and x-ray microscopy [3] took great advantage from the advent of x-ray free-electron lasers (FELs) and, in particular, from their high degree of transverse coherence. In an x-ray FEL, an electron beam with high peak current (up to a few kA), low normalized emittance (<1 mm mrad) and low relative energy spread (<0.1%) is accelerated in a linear accelerator, up to ultrarelativistic velocities. The beam is then injected into an undulator chain (radiator), where the interaction between the electrons and the light they emit ("assisted" by the magnetic field from the undulator itself), leads to the amplification of the latter. Here we consider two distinct modes of FEL operation: one, in which electrons are directly propagated through the radiator, and another, in which they are prebunched following the interaction with an external laser (seed). The first operation mode, called self-amplified spontaneous emission (SASE), results in the generation of high-power (tens of gigawatt) radiation, with tunable energy, up to the hard x-ray spectral range [4–11]. However, in SASE, the initialization of the amplification process occurs from randomly distributed electrons (shot noise) and results in a reduced degree of longitudinal coherence. The latter can be drastically improved when the FEL is seeded [12–20]. The most common externally seeding scheme, called high-gain harmonic generation (HGHG) [21], is the one in which an optical laser imprints an almost monochromatic energy modulation onto the electrons during the interaction in a first short undulator, called modulator. Such a modulation is then converted into density modulation, or "bunching" when the electrons pass through the static magnetic field of a dispersive section. A key point is that substantial

*Corresponding author.
mihai.pop@maxiv.lu.se
†Corresponding author.
giovanni.deninno@elettra.eu

bunching occurs not only at the fundamental (i.e., seed) wavelength, but also at its higher-order harmonics. Finally, the bunched electrons are injected in the radiator, which is tuned to one of the harmonics of the seed, where they emit in phase. Phase-locked emission results in the generation of (almost) transform limited pulses [22–24]. As a condition for this to occur, the bunching level at the considered harmonic must be significantly larger than that due to shot noise, which is present at all frequencies, otherwise the HGHG output gets contaminated by SASE and the longitudinal coherence drastically reduced. Since the bunching level induced by the seed decreases with the harmonic number, this limits the harmonic upshift and, therefore, the shortest wavelength that can be obtained by means of a single HGHG stage [25,26]. For both SASE and HGHG configurations, the light amplification process lasts until when, during the beam propagation in the radiator, the phase matching condition enabling energy transfer from the electrons to the light gets spoiled. When this happens, the process reaches saturation.

Several studies have been carried out in the past, in order to characterize the transverse coherence of SASE [27–32] and HGHG [33,13] FELs. The outcome is that both configurations allow reaching a relatively high degree of coherence. However, while FEL theory and simulations allow for a good theoretical understanding of the principles behind transverse coherence formation, some interesting questions concerning a direct experimental comparison between these configurations remain open: how do the two configurations compare in terms of both maximum achievable transverse coherence and transverse coherence length? How does transverse coherence build up during the amplification process? What is the sensitivity of transverse coherence to a controlled variation of a key working parameter, such as the electron-beam energy spread? In order to address these questions, we have operated the FERMI FEL-2 [22] both in SASE and HGHG regimes, at the same output wavelength (14.8 nm) and with the same electron-beam parameters, and measured the transverse coherence in the two cases.

II. EXPERIMENTAL SETUP

The FERMI FEL normally works in seeded HGHG mode, see Fig. 1(a). For the reasons explained above, in order to reach short (<20 nm) wavelengths, a double HGHG cascade needs to be implemented [22,34]. In such a configuration, the light generated from a first HGHG stage is used to seed a "fresh" portion of the electron beam (i.e., electrons that did not participate to first-stage emission), selected by means of an electron delay line. This triggers the emission process in a second HGHG stage. For the reported experiment, the first HGHG stage was tuned to emit light at 44.4 nm (sixth harmonic of the seed laser), while the second HGHG stage was tuned to 14.8 nm (third

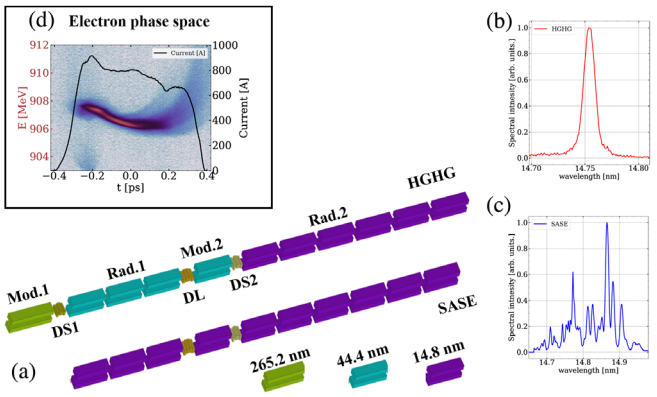

FIG. 1. (a) FERMI FEL operated in HGHG (top) and SASE (bottom) configurations. The layout consists of a first-stage modulator (Mod.1) and a first dispersive section (DS1), only used in HGHG mode, a first-stage radiator made of three undulator sections (Rad.1) a delay line (DL), a second-stage modulator (Mod.2), a second dispersive section (DS2) and finally a second-stage radiator made of six undulator sections (Rad.2). The different undulators are color-coded, based on their resonant wavelength. (b) Typical HGHG and (c) SASE spectra at about 14.8 nm. (d) Electron-beam phase space measured at the end of the linear accelerator.

harmonic of first-stage output). A typical HGHG spectrum obtained at such wavelength is shown in Fig. 1(b). The FERMI FEL can also be operated in SASE mode, see Fig. 1(a). In this scheme, the electron beam is directly injected into the undulator chain (no seed interaction). For the reported experiment, the first-stage radiator, the second-stage modulator and the second-stage radiator were all tuned to 14.8 nm. A significant enhancement of the output emission was obtained by using the delay line and the second-stage dispersive section, in order to boost the bunching (self-) generated during the amplification process [35]. A typical SASE spectrum obtained at around 14.8 nm is shown in Fig. 1(c).

For implementing the two configurations, we prepared an electron beam with the same energy (about 900 MeV), the same peak current (about 1 kA) and energy distribution (slice energy spread: about 100 keV) and used a similar setting of the quadrupoles and magnetic elements determining the electron optics and transport. The electron-beam longitudinal phase space (i.e., time vs energy distribution) that was measured at the end of the linear accelerator is shown in Fig. 1(d). Compared to typical SASE operation, a relatively low peak current has been used in order to limit the growth of microbunching instability and obtain a relatively flat current over a few hundreds of femtoseconds, as well as a smooth energy distribution. These conditions are a prerequisite for an effective double-stage HGHG operation [22], although they set a limit to the maximum SASE output (see next section). However, note that a higher current region is present at the head of the bunch.

Such a region is the one expected to contribute more to light emission in SASE configuration.

In this study, data from one transverse dimension was collected and analyzed to establish a framework for a qualitative comparison between SASE and HGHG transverse coherence properties.

III. ANALYSIS

The degree of transverse coherence was obtained using a Young double-slit setup, see Fig. 2. The interference pattern produced by the slits, spaced by a variable distance, i.e., 0.4, 0.6, 0.8 and 1 mm, was acquired using a CCD. The raw images were processed as follows. First, we found the maximum of the image profile along the vertical direction. Then, we selected a 1D interference pattern at the position of the maximum, by making a cut along the horizontal direction. Such a pattern was then fitted using an analytical function. Its derivation is detailed in the Appendix and is based on the work carried out in [36], using the Fresnel approximation. The function includes several parameters, which are related to the geometry (slit width, slit spacing, distance to CCD) and radiation properties (wavelength, amplitude). It also includes, as a fitting variable, the degree of transverse coherence, γ_{eff}, which is the parameter we are interested in.

By definition, the transverse coherence length is the distance between two points r_1 and r_2, for which $\gamma_{\text{eff}}(r_1, r_2) = e^{-1/2}$. In order to find the transverse coherence length in the x plane, l_{cx}, one can fit γ_{eff} with a Gaussian profile, depending on the slit separation (x) in the x plane:

$$\gamma_{\text{eff}}(x) = \exp\left(-\frac{x^2}{2l_{cx}}\right). \tag{1}$$

Then, given the FEL spot size and the estimated coherence length, one can find the total degree of coherence, ζ_x, for the considered plane. In the frame of the Gauss-Schell model, described in [37], it is possible to decouple the two components ζ_x and ζ_y of the total degree of transverse coherence. The component ζ_x can be expressed in terms of the ratio between the transverse coherence length and the transverse radiation size in the x plane at the position of the slits, $q = l_{cx}/\sigma_x$, as

$$\zeta_x = \frac{1}{\sqrt{1 + 4/q^2}}. \tag{2}$$

For each slit separation and FEL configuration, about 150 shots were recorded. As a measure of goodness of the fit, we used the residual function $R = \frac{\sum (I_{\text{exp}} - I_{\text{fit}})^2}{\sum (I_{\text{exp}})^2}$, where I_{exp} and I_{fit} are, respectively, the experimental and the fitted fringe profiles, thus well-fitted shots have a low R. The average γ_{eff} of each configuration was calculated by taking into account the best fitted 75% shots to avoid contributions from interferograms that could not be fitted properly.

We cross-checked the fitting function [(A10) in the Appendix] with similar functions derived in the Fraunhoffer approximation [23,30,38] and found very good agreement. In Fig. 3, we plot a typical fit for 0.6 mm slit separation. We also estimated the FEL pointing jitter at the slits' position, for both SASE and HGHG, and found it to be 1 order of magnitude smaller than the FEL spot size. We denote the intensities at the two slits I_1 and I_2 respectively. Based on the relation between the effective, γ_{eff} (i.e., measured), and intrinsic degree of coherence, γ, i.e., $\gamma_{\text{eff}} = \frac{2\sqrt{I_1 I_2}}{I_1 + I_2}\gamma$ as described in [29], we expect our estimates of γ to be reduced by less than 1% due to unequal illumination of the two slits due to pointing jitter.

A finite temporal coherence in a Young double-slit experiment may have the effect of reducing fringe visibility (and, therefore, the estimated γ_{eff}) at the points in the

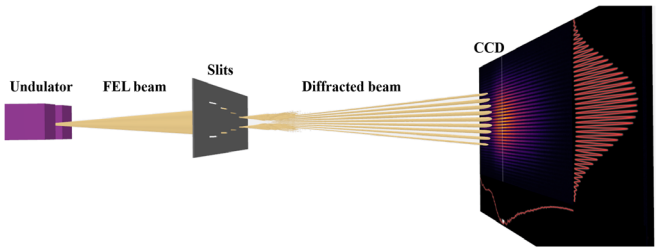

FIG. 2. Young's double-slit setup used to measure transverse coherence. After the last radiator section, the photon pulse reaches the slits. For the experiment, we used slits with different separations, i.e., 0.4, 0.6, 0.8 and 1 mm, placed symmetrically with respect to the center of the beam spot, whose dimension was about 3 mm (FWHM). The pulse diffracted by the slits was recorded using a CCD of 1024 by 1024 pixels, with pixel width of 13.3 μm. The distance between the slits and the CCD was about 8.6 m.

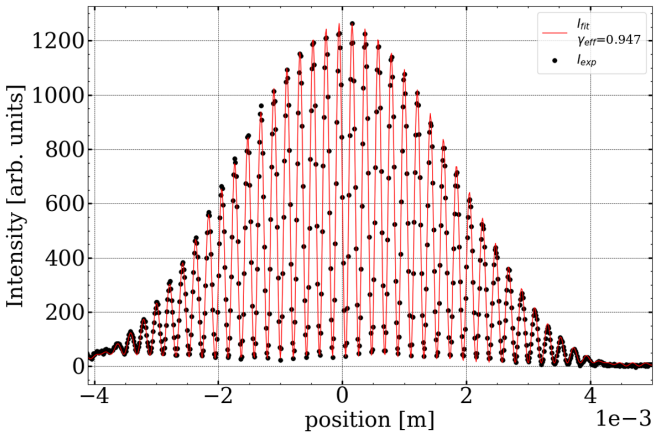

FIG. 3. Example of fitting the 1D experimental interference pattern (black dots) with the analytical function given in Eq. (A10) for the SASE full undulator chain, and for the case of 0.6 mm slit separation.

interference pattern where the path delay between the light coming from the two slits is comparable with (or larger than) the longitudinal coherence length. We estimate the coherence time as $t_c = 1/\Delta\nu$, where $\Delta\nu$ is the rms spectral width. The longitudinal coherence length is simply $l_{long} = t_c c$, where c is the speed of light. We focus the analysis of this effect on the SASE mode of operation because, as seen in Figs. 1(b) and 1(c), the bandwidth of HGHG is 1 order of magnitude smaller than the corresponding values for SASE, and therefore the longitudinal coherence length is 1 order of magnitude larger. In our experiment, we measured a typical coherence length for SASE of about 2.9 μm. The path delay of the light coming from slits separated by 0.8 mm, 4 mm away from the center intensity on the CCD is $\Delta l = 0.46$ μm. Based on the fact that l_{long} is significantly larger at Δl, we can assume that the interplay between transverse and longitudinal coherence is, in our case, negligible.

The energy chirp present in the beam [Fig. (1a)] can lead to an underestimation of the longitudinal coherence length by broadening the bandwidth. Electrons from the head and middle of the beam have different energies and thus radiate at different resonant wavelengths. We estimate that due to our chirp the electrons in the head and middle of the electron phase space, −0.2 and 0 ps in Fig. 1(d) respectively, have an energy difference of 1.5 MeV. This energy difference will produce a wavelength shift of 0.02 nm which is well within our SASE bandwidth. Furthermore, since the tendency is to underestimate the longitudinal coherence length, our assumption that we can neglect the effect of longitudinal coherence effects on the transverse coherence measurements is strengthened.

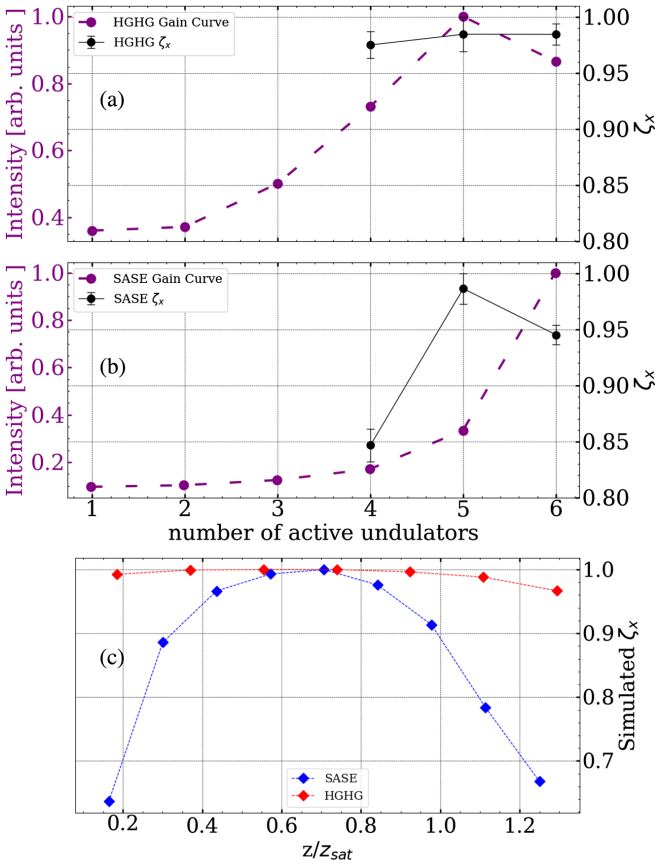

FIG. 4. Gain curve (purple) and total degree of transverse coherence ζ_x (black) (normalized to unity), as a function of the distance in the second-stage radiator, for (a) HGHG and (b) SASE. Simulated total degree of transverse coherence for SASE (blue) and HGHG (red) (c).

IV. RESULTS

Figure 4 shows the growth of the FEL power (gain curve) and the total degree of transverse coherence, ζ_x (here normalized to its maximum), as a function of the number of radiator segments tuned on resonance, for both HGHG and SASE configurations. The measurements have been performed by progressively tuning the radiator sections to the resonant wavelength, and acquiring, for a given number of active radiator sections, the average output power of around 50 shots and the corresponding interference patterns from different slit separations. The curves showing the gain in power are deliberately left without error bars as they serve only to estimate the stage of the amplification process at which each coherence measurement was taken. Due to the low signal generated when only a few radiator sections were tuned, we have been able to collect the interferograms only in the case in which at least four undulators in the second radiator [RAD.2 in Fig. 1(a)] were active.

As it can be seen in Fig. 4(a), a proper setting of the dispersive sections and of the delay line allows the HGHG gain curve (in red) to reach power saturation before the last radiator module. Note that the trend of the total degree of transverse coherence (plotted in black), measured using four, five and six radiator sections is almost constant and saturates before the intensity. This result is in qualitative agreement with the simulation shown in the Fig. 4(c), where the total degree of transverse coherence is calculated [39] from the complex field generated by the numerical code GENESIS1.3 [40].

Instead, the FEL did not reach power saturation operating in SASE OK mode, see Fig. 4(b). Based on the calculation of the gain length obtained from the exponential fit of the gain curve, we estimate that SASE saturation could have been reached, if two additional radiator sections were available. However, as analytically predicted in [28], and through simulations in [39], the transverse SASE coherence can be assumed to saturate at about 77% of the power saturation position. The results reported in Fig. 4(b) show that the total degree of transverse coherence reaches maximum value well before intensity saturation. Consistently with the simulations shown in Fig. 4(c), The reported results provide a first experimental confirmation of the early saturation of transverse coherence in SASE. This allows us to draw a direct

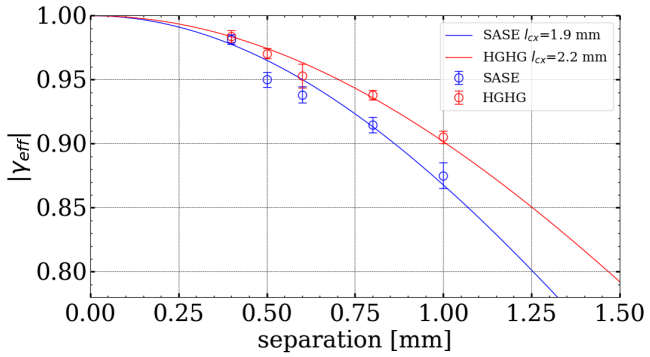

FIG. 5. The degree of transverse coherence γ_{eff} as a function of slit separation, for SASE (blue circles) and HGHG (red circles) and the fit for Gaussian decay HGHG (red) and SASE (blue) solid lines providing the transverse coherence lengths.

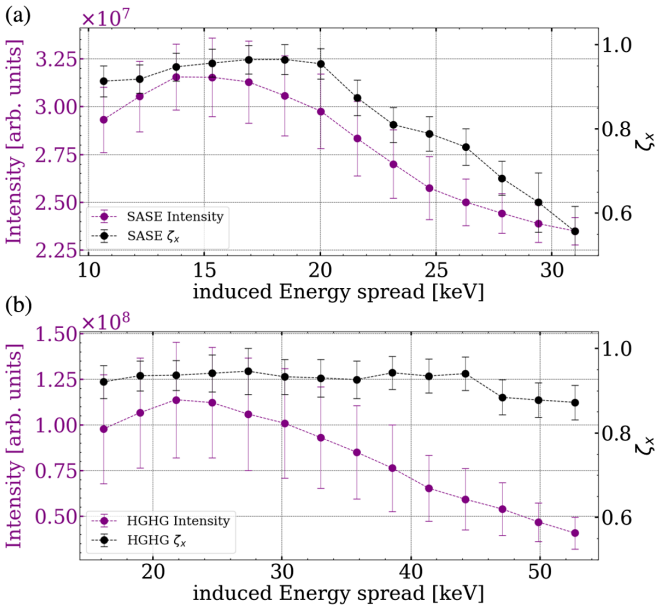

FIG. 6. Normalized total degree of coherence ζx (black) and intensity (purple) in SASE (a) and HGHG (b) configurations, as a function of LH-induced energy spread at the laser heater position, before compression.

comparison between the maximum degree of coherence reached in HGHG and SASE configurations.

A quantitative comparison between the degree of transverse coherence, γ_{eff}, obtained in HGHG and SASE configurations is reported in Fig. 5. The trend shows that, while at the smallest slit separation the degree of transverse coherence is virtually the same, for larger separation the degree of transverse coherence obtained in HGHG is higher. In other words, HGHG is characterized by a larger transverse coherence length. We note here that we measured the transverse size of the FEL beam in HGHG and SASE modes, and found $\sigma_x^{\text{SASE}} \approx 1.25 \pm 0.05$ mm $\sigma_x^{\text{HGHG}} \approx 1.38 \pm 0.1$ mm. Fitting γ_{eff} (x) to Eq. (1), we obtained transverse coherence lengths of $l_{cx}^{\text{SASE}} = 1.93 \pm 0.02$ and $l_{cx}^{\text{HGHG}} = 2.20 \pm 0.01$ mm. Using Eq. (2) we calculate similar total degrees of transverse coherence $\zeta_x^{\text{SASE}} = 0.60 \pm 0.03$ and $\zeta_x^{\text{HGHG}} = 0.62 \pm 0.02$ for SASE and HGHG, respectively.

Finally, we studied the sensitivity of the total degree of transverse coherence to the electron-beam energy spread. The latter was varied by means of a laser heater (LH) system, which is normally used to slightly increase the effective energy spread during the early part of electrons' acceleration in order to avoid the detrimental effects on SASE [41] and HGHG [42] emission due to self-induced microbunching instability. Figure 6 shows the behavior of HGHG and SASE total degree of transverse coherence, normalized to the maximum value, for different values of LH-induced energy spread. Both configurations show sensitivity to microbunching, which needs to be reduced by means of an appropriate tuning of the LH energy and in both cases the maxima of transverse coherence and FEL intensity occur near the same LH-induced energy spread. Notably, the degree of transverse coherence for the case of HGHG remains constant also for LH energies larger than optimum, which result in a reduced FEL intensity. This can be explained by looking at the dependence of total degree of transverse coherence along the amplification process, for both HGHG and SASE configurations. Indeed, while for SASE the total degree of transverse coherence is built through the mode selection taking place during the amplification process [28], in HGHG the total degree of transverse coherence, as the longitudinal one, is driven by the seed laser and, therefore, is already close to maximum when the electron beam starts emitting coherently at the entrance of the radiator. For this reason, also when the energy spread induced by the LH is large enough to inhibit the FEL exponential growth, the total degree transverse coherence in HGHG configuration is virtually not affected.

V. CONCLUSIONS

We have shown that, when operated at the same wavelength and with the same electron-beam conditions, seeded and unseeded free-electron lasers can reach a similar total degree of transverse coherence. Our results demonstrate that the process through which coherence is built is fundamentally different in the two cases. Indeed, in the case of seeded harmonic generation, coherence is inherited from the seed laser and does not rely on the amplification process to develop. The latter is instead essential to drive mode selection in the unseeded case, although maximum coherence is reached well before power saturation.

Data underlying the results presented in this paper are not publicly available at this time but may be obtained from the authors upon reasonable request.

The authors declare no conflicts of interest.

APPENDIX: DERIVATION OF THE INTENSITY PROFILE FROM A YOUNG DOUBLE-SLIT EXPERIMENT IN THE FRESNEL APPROXIMATION

We assume a spherical incoming wave,

$$\frac{E_0\exp(-ikr_1)}{r_1}=\frac{E_0\exp[-ik(z_1+\frac{x_1^2}{2z_1})]}{z_1}\quad\text{with}\quad r_1=\sqrt{z_1^2+x_1^2},$$

is diffracted by a double slit at distance z_1 from the focus. The field after the two slits is given by

$$E(x_1)=\left\{\begin{array}{ll}\frac{E_0\exp[-ik(z_1+\frac{x_1^2}{2z_1})]}{z_1}, & \text{for } x\in\left(\pm\frac{d}{2}-\frac{w_{\text{slit}}}{2},\pm\frac{d}{2}+\frac{w_{\text{slit}}}{2}\right)\\ 0, & \text{otherwise}\end{array}\right\}. \tag{A1}$$

The field at the plane of the screen (x_2) is just the superposition $\vec{E}=\vec{E_1}+\vec{E_2}$, where $\vec{E_j}$ is the complex field from slit j propagated a distance z to the plane of the screen. According to the Huygens-Fresnel principle the field at plane x_2 is

$$E(x_2)=\sqrt{\frac{k}{2\pi iz}}\exp(ikz)\times\int_{-\infty}^{\infty}E(x_1)\exp\left[\frac{ik(x_1-x_2)^2}{2z}\right]dx, \tag{A2}$$

where $E(x_1)$ is the field at the plane x_1 (the plane of the slits). We write the explicit field at the x_2 plane (the plane of the CCD screen)

$$E(x_2)=\sqrt{\frac{k}{2\pi iz}}\frac{\exp[ik(z-z_0)]}{z_0}E_0\times\left\{\int_{-\frac{d}{2}-\frac{w_{\text{slit}}}{2}}^{-\frac{d}{2}+\frac{w_{\text{slit}}}{2}}\exp\left[\frac{ik(x_1-x_2)^2}{2z}+\frac{ikx_1^2}{z0}\right]dx+\int_{-\frac{d}{2}-\frac{w_{\text{slit}}}{2}}^{-\frac{d}{2}+\frac{w_{\text{slit}}}{2}}\exp\left[\frac{ik(x_1-x_2)^2}{2z}+\frac{ikx_1^2}{z0}\right]dx\right\}. \tag{A3}$$

The first integral corresponds to E_1 and the second one to E_2. To be able to reach a simple solvable equation we write the exponential under the integrals in the form

$$E(x_2)=A\left[\int_0^{w_{12}}\exp\left(i\frac{\varphi^2}{2}\pi\right)dx-\int_0^{w_{11}}\exp\left(i\frac{\varphi^2}{2}\pi\right)dx+\int_0^{w_{22}}\exp\left(i\frac{\varphi^2}{2}\pi\right)dx-\int_0^{w_{21}}\exp\left(i\frac{\varphi^2}{2}\pi\right)dx\right]. \tag{A4}$$

These integrals are commonly known as *Fresnel integrals* and take the notation

$$\int_0^w\exp\left(i\frac{\varphi^2}{2}\pi\right)d\varphi=\int_0^w\cos\left(\frac{\varphi^2}{2}\pi\right)d\varphi+i\int_0^w\sin\left(\frac{\varphi^2}{2}\pi\right)d\varphi=C(w)+iS(w). \tag{A5}$$

Carrying out the algebra we find that

$$\varphi=\sqrt{\frac{k(z_0-z)}{zz_0\pi}}\left(x_1-x_2\frac{z_0}{z_0-z}\right)$$

and an extra phase term

$$\varphi_{\text{extra}}=ik\frac{x_2}{z_0-z}$$

which does not depend on x_1 and can thus be incorporated in the complex amplitude outside the integrals. The new limits of integration are

$$\begin{aligned}w_{11}&=\sqrt{\frac{k(z_0-z)}{zz_0\pi}}\left(-\frac{d}{2}-\frac{w_{\text{slit}}}{2}-x_2\frac{z_0}{z_0-z}\right)\\ w_{12}&=\sqrt{\frac{k(z_0-z)}{zz_0\pi}}\left(-\frac{d}{2}+\frac{w_{\text{slit}}}{2}-x_2\frac{z_0}{z_0-z}\right)\\ w_{21}&=\sqrt{\frac{k(z_0-z)}{zz_0\pi}}\left(\frac{d}{2}-\frac{w_{\text{slit}}}{2}-x_2\frac{z_0}{z_0-z}\right)\\ w_{22}&=\sqrt{\frac{k(z_0-z)}{zz_0\pi}}\left(\frac{d}{2}+\frac{w_{\text{slit}}}{2}-x_2\frac{z_0}{z_0-z}\right).\end{aligned} \tag{A6}$$

To reduce the notation complexity we make the following substitutions:

$$\int_0^{w_{jk}}\exp\left(i\frac{\varphi^2}{2}\pi\right)d\varphi=C_{jk}+iS_{jk}\quad\text{and}\quad A=\sqrt{\frac{k}{i2z\pi}}\frac{\exp[ik(z-z_0)]\exp[\frac{ikx_2^2}{z_0-z}]}{z_0}.$$

A further simplifying notation $C_{i2}-C_{i1}=C_i$ and $S_{i2}-S_{i1}=S_i$ gives a simple closed form for the field at plane x_2:

$$E(x_2, z) = A(C_1 + iS_1 + C_2 + iS_2). \tag{A7}$$

Identifying the components with the field originating from the two slits we find $E_i = A(C_i + iS_i)$.

The time average intensity is the measurable at the x_2 plane:

$$I = \langle |E_1 + E_2|^2 \rangle = \langle |E_1|^2 \rangle + \langle |E_2|^2 \rangle + \langle E_1 E_2^* \rangle + \langle E_2 E_1^* \rangle. \tag{A8}$$

The mutual coherence function is defined as

$$G(r_1, r_2, \tau) = \langle E^*(r_1, t+\tau) E(r_2, t) \rangle.$$

For quasimonochromatic sources the mutual intensity function $G(r_1, r_2, \tau = 0) = G_{12}$ or its scaled version $\gamma_{12} = G_{12}/\sqrt{I_1 I_2}$ referred to as the complex degree of transverse coherence, is used to describe the coherence in the transverse plane.

Introducing this notation in Eq. (A7) we find

$$I = I_1 + I_2 + 2\,\mathrm{Re}\{G_{12}\} = I_1 + I_2 + 2\sqrt{I_1 I_2}\,\mathrm{Re}\{\gamma\}$$

or

$$I = I_1 + I_2 + 2\sqrt{I_1 I_2}|\gamma| \cos\theta, \tag{A9}$$

where $\cos\theta = \mathrm{Re}\{G_{12}\}/|G_{12}|$. θ is the phase of the complex valued G_{12}.

Carrying out the math we identify

$$I_i = \langle |E_i|^2 \rangle = |A|^2 (C_i^2 + iS_i^2)$$

$$G_{12} = \langle |E_2 E_1^*|^2 \rangle = |A|^2 [C_1 C_2 + S_1 S_2 + i(C_1 S_2 - C_2 S_1)]$$

$$\mathrm{Re}\{G_{12}\} = |A|^2 (C_1 C_2 + S_1 S_2)$$

$$|G_{12}| = |A|^2 \sqrt{C_1^2 C_2^2 + S_1^2 S_2^2 + C_1^2 S_2^2 + S_1^2 C_2^2}.$$

Finally we have the closed form intensity in terms of C_i, S_i and γ:

$$I = |A|^2 [C_2^2 + C_1^2 + S_2^2 + S_1^2 + |\gamma|(C_1 C_2 + S_1 S_2)]. \tag{A10}$$

The previous relation was utilized to fit the 1D interference patterns obtained from the CCD images (see Sec. III).

[1] H. N. Chapman, A. Barty, M. J. Bogan, S. Boutet, M. Frank, S. P. Hau-Riege *et al.*, Femtosecond diffractive imaging with a soft-x-ray free-electron laser, Nat. Phys. **2**, 839 (2006).

[2] T. Gorkhover, A. Ulmer, K. Ferguson, M. Bucher, F. R. N. C. Maia, J. Bielecki *et al.*, Femtosecond x-ray Fourier holography imaging of free-flying nanoparticles, Nat. Photonics **12**, 150 (2018).

[3] C. J. Jacobsen, X-ray microscopy using FELs: Possibilities and challenges, in *Biomedical Applications of Free-Electron Lasers* (Society of Photo-Optical Instrumentation Engineers (SPIE), San Jose, CA, 2000), Vol. 3925, pp. 16–25.

[4] R. Bonifacio, C. Pellegrini, and L. M. Narducci, Collective instabilities and high-gain regime free electron laser, *AIP Conf. Proc.* 118, 236 (1984).

[5] E. Saldin, E. V Schneidmiller, and M. V Yurkov, *The Physics of Free Electron Lasers* (Springer Science and Business Media, Berlin, Germany, 1999).

[6] V. Ayvazyan, N. Baboi, I. Bohnet, R. Brinkmann, M. Castellano, P. Castro *et al.*, Generation of GW Radiation Pulses from a VUV Free-Electron Laser Operating in the Femtosecond Regime, Phys. Rev. Lett. **88**, 104802 (2002).

[7] W. Ackermann, G. Asova, V. Ayvazyan, A. Azima, N. Baboi, J. Bähr *et al.*, Operation of a free-electron laser from the extreme ultraviolet to the water window, Nat. Photonics **1**, 336 (2007).

[8] P. Emma, R. Akre, J. Arthur, R. Bionta, C. Bostedt, J. Bozek *et al.*, First lasing and operation of an Ångstrom-wavelength free-electron laser, Nat. Photonics **4**, 641 (2010).

[9] T. Ishikawa, H. Aoyagi, T. Asaka, Y. Asano, N. Azumi, T. Bizen *et al.*, A compact x-ray free-electron laser emitting in the sub-Ångström region, Nat. Photonics **6**, 540 (2012).

[10] A. M. Kondratenko and E. L. Saldin, Generation of coherent radiation by a relativistic electron beam in an ondulator, Part. Accel. **10**, 207 (1980), http://cds.cern.ch/record/1107977/files/p207.pdf.

[11] H.-S. Kang, C.-K. Min, H. Heo, C. Kim, H. Yang, G. Kim *et al.*, Hard x-ray free-electron laser with femtosecond-scale timing jitter, Nat. Photonics **11**, 708 (2017).

[12] L.-H. Yu, M. Babzien, I. Ben-Zvi, L. F. DiMauro, A. Doyuran, W. Graves *et al.*, High-gain harmonic-generation free-electron laser, Science **289**, 932 (2000).

[13] E. Allaria, R. Appio, L. Badano, W. A. Barletta, S. Bassanese, S. G. Biedron *et al.*, Highly coherent and stable pulses from the FERMI seeded free-electron laser in the extreme ultraviolet, Nat. Photonics **6**, 699 (2012).

[14] P. R. Ribič, A. Abrami, L. Badano, M. Bossi, H.-H. Braun, N. Bruchon *et al.*, Coherent soft x-ray pulses from an echo-enabled harmonic generation free-electron laser, Nat. Photonics **13**, 555 (2019).

[15] G. Lambert, T. Hara, D. Garzella, T. Tanikawa, M. Labat, B. Carre *et al.*, Injection of harmonics generated in gas in a free-electron laser providing intense and coherent extreme-ultraviolet light, Nat. Phys. **4**, 296 (2008).

[16] T. Togashi, E. J. Takahashi, K. Midorikawa, M. Aoyama, K. Yamakawa, T. Sato *et al.*, Extreme ultraviolet free electron laser seeded with high-order harmonic of Ti: sapphire laser, Opt. Express **19**, 317 (2011).

[17] T. Inagaki, T. Tanaka, N. Adumi, T. Hara, R. Kinjo, H. Maesaka *et al.*, Hard x-ray self-seeding set-up and results at SACLA, in *Proceedings of the 2014 FEL Conference, Basel, Switzerland, TUC01* (JACoW, Geneva, Switzerland, 2014).

[18] J. Amann, W. Berg, V. Blank, F.-J. Decker, Y. Ding, P. Emma *et al.*, Demonstration of self-seeding in a hard-x-ray free-electron laser, Nat. Photonics **6**, 693 (2012).

[19] I. Inoue, T. Osaka, T. Hara, T. Tanaka, T. Inagaki, T. Fukui *et al.*, Generation of narrow-band x-ray free-electron laser via reflection self-seeding, Nat. Photonics **13**, 319 (2019).

[20] I. Nam, C.-K. Min, B. Oh, G. Kim, D. Na, Y. J. Suh *et al.*, High-brightness self-seeded x-ray free-electron laser covering the 3.5 KeV to 14.6 KeV range, Nat. Photonics **15**, 435 (2021).

[21] L. H. Yu, Generation of intense UV radiation by subharmonically seeded single-pass free-electron lasers, Phys. Rev. A **44**, 5178 (1991).

[22] E. Allaria, D. Castronovo, P. Cinquegrana, P. Craievich, M. Dal Forno, M. B. Danailov *et al.*, Two-stage seeded soft-x-ray free-electron laser, Nat. Photonics **7**, 913 (2013).

[23] G. De Ninno, D. Gauthier, B. Mahieu, P. R. Ribič, E. Allaria, P. Cinquegrana *et al.*, Single-shot spectro-temporal characterization of XUV pulses from a seeded free-electron laser, Nat. Commun. **6**, 8075 (2015).

[24] D. Gauthier, P. R. Ribič, G. De Ninno, E. Allaria, P. Cinquegrana, M. B. Danailov, A. Demidovich, E. Ferrari, and L. Giannessi, Generation of Phase-Locked Pulses from a Seeded Free-Electron Laser, Phys. Rev. Lett. **116**, 024801 (2016).

[25] E. Allaria and G. De Ninno, Soft-X-Ray Coherent Radiation Using a Single-Cascade Free-Electron Laser, Phys. Rev. Lett. **99**, 014801 (2007).

[26] G. Penco, G. Perosa, E. Allaria, S. Di Mitri, E. Ferrari, L. Giannessi, S. Spampinati, C. Spezzani, and M. Veronese, Enhanced seeded free electron laser performance with a "cold" electron beam, Phys. Rev. Accel. Beams **23**, 120704 (2020).

[27] R. Ischebeck, J. Feldhaus, C. Gerth, E. Saldin, P. Schmüser, E. Schneidmiller *et al.*, Study of the transverse coherence at the TTF free electron laser, Nucl. Instrum. Methods Phys. Res., Sect. A **507**, 175 (2003).

[28] E. L. Saldin, E. A. Schneidmiller, and M. V Yurkov, Statistical and coherence properties of radiation from x-ray free-electron lasers, New J. Phys. **12**, 035010 (2010).

[29] I. A. Vartanyants, A. Singer, A. P. Mancuso, O. M. Yefanov, A. Sakdinawat, Y. Liu *et al.*, Coherence Properties of Individual Femtosecond Pulses of an X-Ray Free-Electron Laser, Phys. Rev. Lett. **107**, 144801 (2011).

[30] A. Singer, F. Sorgenfrei, A. P. Mancuso, N. Gerasimova, J. Gulden, T. Gorniak *et al.*, Spatial and Temporal Coherence Properties of Single Free-Electron Laser Pulses, Opt. Express **20**, 17480 (2012).

[31] E. A. Schneidmiller and M. V. Yurkov, Coherence properties of the radiation from FLASH, J. Mod. Opt. **63**, 293 (2016).

[32] T. Wodzinski, M. Mehrjoo, M. Ruiz-Lopez, B. Keitel, M. Kuhlmann, M. Brachmanski *et al.*, Single-shot transverse coherence measurements with Young's double pinholes at FLASH2, J. Phys. Commun. **4**, 75014 (2020).

[33] O. Y. Gorobtsov, G. Mercurio, F. Capotondi, P. Skopintsev, S. Lazarev, I. A. Zaluzhnyy *et al.*, Seeded x-ray free-electron laser generating radiation with laser statistical properties, Nat. Commun. **9**, 4498 (2018).

[34] E. Allaria, L. Badano, S. Bassanese, F. Capotondi, D. Castronovo, P. Cinquegrana *et al.*, The FERMI free-electron lasers, J. Synchrotron Radiat. **22**, 485 (2015).

[35] G. Penco, E. Allaria, G. De Ninno, E. Ferrari, and L. Giannessi, Experimental Demonstration of Enhanced Self-Amplified Spontaneous Emission by an Optical Klystron, Phys. Rev. Lett. **114**, 013901 (2015).

[36] V. F. Klimkin and G. N. Sankin, Lecture demonstration of Fresnel diffraction by a slit and half-plane, Russ. Phys. J. **48**, 559 (2005).

[37] I. A. Vartanyants and A. Singer, Coherence properties of hard x-ray synchrotron sources and x-ray free-electron lasers, New J. Phys. **12**, 035004 (2010).

[38] D. Cho, J. Yang, S. Kim, D. Nam, J. Park, S. Kim, K. Tono, M. Yabashi, T. Ishikawa, and C. Song, Comparing the spatial coherence of the natural and focused x-rays from a free electron laser, Opt. Express **27**, 19573 (2019).

[39] Y. Ding, Z. Huang, S. A. Ocko *et al.*, Transverse-coherence properties of the FEL at the LCLS, Report No. SLAC-PUB-14235, 2010, https://www.slac.stanford.edu/pubs/slacpubs/14000/slac-pub-14235.pdf.

[40] S. Reiche, GENESIS1.3: A fully 3D time-dependent FEL simulation code, Nucl. Instrum. Methods Phys. Res., Sect. A **429**, 243 (1999).

[41] C. Lechner, A. Azima, M. Drescher, T. Maltezopoulos, V. Miltchev, T. Plath *et al.*, Demonstration of SASE suppression through a seeded microbunching instability, in *Proceedings of the 36th International Free-Electron Laser Conference, Basel* (JACoW, Geneva, Switzerland, 2014), pp. 177–180.

[42] S. Spampinati, E. Allaria, L. Badano, S. Bassanese, S. Biedron, D. Castronovo *et al.*, Laser heater commissioning at an externally seeded free-electron laser, Phys. Rev. ST Accel. Beams **17**, 120705 (2014).